Supplementary Material: Higgs oscillations in a unitary Fermi superfluid

September 18, 2023

Contents

1 Experimental protocol

1.1 Sample Preparation

In our experiments, we cool a balanced mixture of fermionic ^{6}Li atoms in the $|F = 1/2, m_\mathrm{F} = \pm 1/2\rangle (\equiv |1\rangle - |2\rangle$, blue circles in Fig. 2, main text) or $|F = 1/2, m_\mathrm{F} = 1/2\rangle - |F = 3/2, m_\mathrm{F} = -3/2\rangle (\equiv |1\rangle - |3\rangle$, green squares) hyperfine states in a 100 W, 1075 nm single beam optical dipole trap. Degeneracy is reached through evaporative cooling by smoothly lowering the trap laser power at the magnetic field where the s-wave scattering length diverges, $a \to \infty$. Subsequently, the atom cloud is transferred to an oblate harmonic potential, formed by a combination of optical and magnetic fields. The oblate trap is formed between two anti-nodes of a cylindrically focused, 532-nm (blue-detuned), TEM_{01} mode laser beam [1–3], where the two anti-nodes are separated by ≈ 90 μm propagating along the y-direction and the $1/\mathrm{e}^2$ radius in the x-direction is ≈ 1.0 mm. The optical potential produces the confinement in the z direction and a very weak anti-confinement in the x-y plane. The residual magnetic field curvature from the Feshbach coils provides highly harmonic and cylindrically symmetric confinement in the x-y plane, which dominates the anti-trapping of the optical potential. The measured trapping frequencies are $\omega_z/2\pi = 105$ Hz(1) and $(\omega_x, \omega_y) = 2\pi \times (24.5, 24.5)$ Hz at a magnetic field of $B = 832.2$ G (corresponding to the $|1\rangle - |2\rangle$ Feshbach resonance [4]). The asymmetry in the trapping potential is $|\omega_x - \omega_y|/\omega_r \lesssim 0.01$. Note that $\omega_r \propto \sqrt{B}$ so the radial confinement also changes when we tune interactions. Typically, we produce clouds with temperatures of 0.09 T/T_F, where T_F is the Fermi temperature and $N =$

3×10^5 atoms per spin state.

To determine the temperature of the atom clouds (horizontal axis of Figs. 2 and 3 in the main text) we follow the quench procedure as described in the main text, however, instead of probing the clouds with Bragg lasers following the quench the cloud is held for 500 ms and an $in-situ$ absorption image is taken (after this hold time, no dynamics in the density distribution are detected [5]). The temperature can be determined by fitting the known equation of state (EoS) for the pressure of a unitary Fermi gas [6] to the line densities of a trapped atom cloud at equilibrium. Throughout this study we probe temperatures ranging from 0.1 to 0.18 T/T_{F}. The higher temperatures are obtained by varying the endpoint of the initial evaporative cooling process, which loads a higher temperature cloud into the oblate trapping potential and the temperature is extracted following the same procedure described above.

1.2 Bragg Spectroscopy Calibration

The post-quench dynamics are probed using two tightly-focused Bragg laser beams, as shown in Fig. 1(a), that intersect in the centre of the cloud where the density is near-uniform [7, 8]. Two-photon Bragg spectroscopy is both energy and momentum selective thus, by setting the frequency difference to half of the atomic recoil frequency ($\omega_r/2 = \hbar k^2/4m$), pairs with zero center-of-mass momentum are resonantly excited [8, 9]. These pairs then begin moving with a velocity $\hbar\mathbf{k}/m$ where, $\mathbf{k} = \mathbf{k}_a - \mathbf{k}_b$ is the difference of the wave-vectors of the two Bragg lasers. We use $k \simeq 4k_F$ to ensure that ω is large compared to E_{F}, and the pulse duration (50 μs) is relatively short with respect to the dynamics. The center of mass displacement ΔX_{CoM} following time-of-flight expansion, reveals the momentum imparted to the atoms by the Bragg lasers. Fig. 1(b) shows an absorption image of an atom cloud following the experimental sequence described in the main text. A large number of atoms are seen to be displaced from the centre of the cloud towards the right of the image. The crescent shape in Fig. 1(b) is a result of collisions between scattered atoms and the unperturbed atoms in the cloud which occur following the Bragg pulse [10].

We have measured the sensitivity of the centre of mass displacement, ΔX_{CoM} at unitarity as the pair condensate fraction varies. To determine the centre of mass displacement, ΔX_{CoM}, we prepare clouds at a range of initial temperatures by varying the endpoint of the evaporation and then applying a Bragg pulse (to the clouds at equilibrium) and measure the response as described above. To determine the pair condensate fraction a degenerate cloud at 832.2 G is produced at a given temperature and in equilibrium. Subsequently, we jump the magnetic field far onto the BEC side of the Feshbach resonance in ≈ 50 μs and simultaneously turn off the optical (z) confinement. The weakly bound pairs are converted to tightly bound molecules, whose centre of mass momentum is preserved [11]. The weakly interacting molecules then expand ballistically along z before the magnetic field is ramped back to 832.2 G in 2.5 ms to dissociate the molecules. The total expansion time is approximately one quarter of the radial trapping period, to best reveal the momentum distribution. Finally, an absorption image is taken and fitted with a bi-modal distribution to determine the condensate fraction.

Fig. 1(c) shows the response of the ΔX_{CoM} of the cloud as the pair condensate fraction, and therefore the temperature, is varied. As the condensate fraction is reduced, the centre of mass displacement, ΔX_{CoM} also decreases. The Bragg signal shows a clear dependence on the condensate fraction, which reflects the change in the number of condensed pairs available to take part in the scattering process.

1.3 Determination of Density

To observe the Higgs oscillation most clearly the Bragg scheme addresses atoms at the centre of the trap, where the density is near homogeneous, as in previous studies [7, 8]. We define the mean density $\bar{n}$ in the Bragg volume as

$$\bar{n} = \frac{\int \Omega_{\mathrm{Br}}(\mathbf{r}) n(\mathbf{r}) \mathrm{d}^3\mathbf{r}}{\int \Omega_{\mathrm{Br}}(\mathbf{r}) \mathrm{d}^3\mathbf{r}}, \tag{1}$$

where $\Omega_{\mathrm{Br}}(\mathbf{r})$ is the spatially dependent two-photon Rabi frequency, which is proportional to the geometric mean of the intensities of the two laser beams $\sqrt{I_a(\mathbf{r})I_b(\mathbf{r})}$ and $n(\mathbf{r})$ is the 3D density distribution. The mean density sets the relevant energy scale and the Higgs oscillation frequency

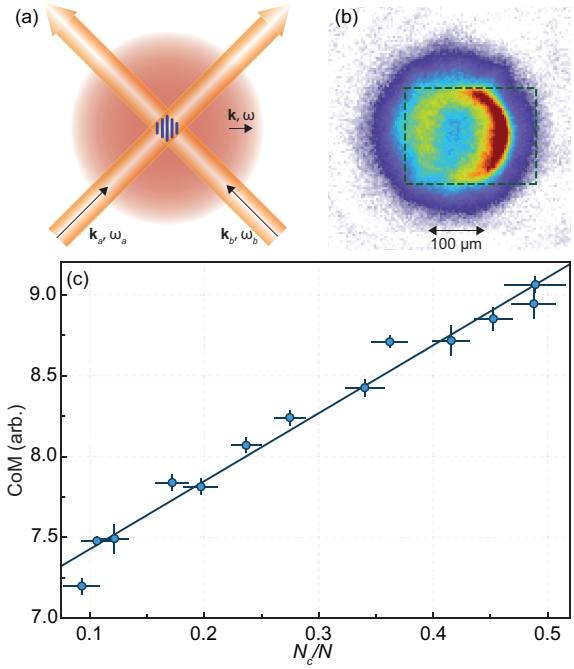

Figure 1: (Color online) (a) Schematic of the experimental setup for focused beam Bragg spectroscopy. Two laser beams with wave vectors $\mathbf{k}_a$ and $\mathbf{k}_b$ and frequencies ω_a and ω_b are focused into the center of a trapped atom cloud. The beams have a $1/e^2$ radius of 15 μm and intersect at an angle of $2\theta = 72.6^\circ$ (b) Absorption image of an atom cloud following an excitation with a Bragg frequency $\omega/(2\pi) = +50$ kHz. The dashed rectangle indicates the region used for determination of the centre of mass displacement. (c) Measured center of mass displacement, ΔX_{CoM} as a function of measured pair condensate fraction.

via Fermi energy $E_{\mathrm{F}} = \frac{\hbar}{2m}(3\pi^2\bar{n})^{2/3}$, and the normalized frequency $\hbar\omega_{\mathrm{H}}/2E_{\mathrm{F}}$, where m is the atomic mass and ω_{H} is the Higgs oscillation frequency.

To determine the mean density, the true (3D) density distribution $n(\mathbf{r})$ of the trapped cloud and the intensity product of the Bragg laser beams with their intersecting Gaussian spatial profiles are combined. The 3D density $n(\mathbf{r})$ is extracted through applying an inverse Abel transform to absorption images of unperturbed trapped clouds. Images of trapped clouds are taken using a high intensity ($I/I_{\mathrm{sat}} > 10$) and short imaging pulse length of 1 μs. The inverse Abel transform method uses a Fourier decomposition where the radial density distribution is expanded in a Fourier series. This method requires no direct differentiation and allows reconstruction of the central density without singularities. From this, we are able to determine $\bar{n}$ with an error of approximately 7.5 %, which leads to a 5 % error in the Fermi energy.

In Fig. 2, we plot the direct measured centre of mass displacement (ΔX_{CoM}) vs. time along with the fitted sinusoid, for the same data as in Fig. 2 of the main text. These traces show how the total Bragg signal decreases with increasing temperature, the magnitude of the oscillations falls off with increasing temperatures and the frequency changes for clouds prepared at different temperatures. In Fig 2(a) the hold time is in ms and in 2(b) in units of the local Fermi time $\tau_F = \hbar/E_F$. The absolute oscillation frequency is set by the local Fermi energy, which in turn is set by the local density. Clouds at different temperatures may have different densities due to changes in the preparation sequence. This leads to the variations in the absolute oscillation frequency in (a), which become more consistent when plotted as a function of the scaled time in (b).

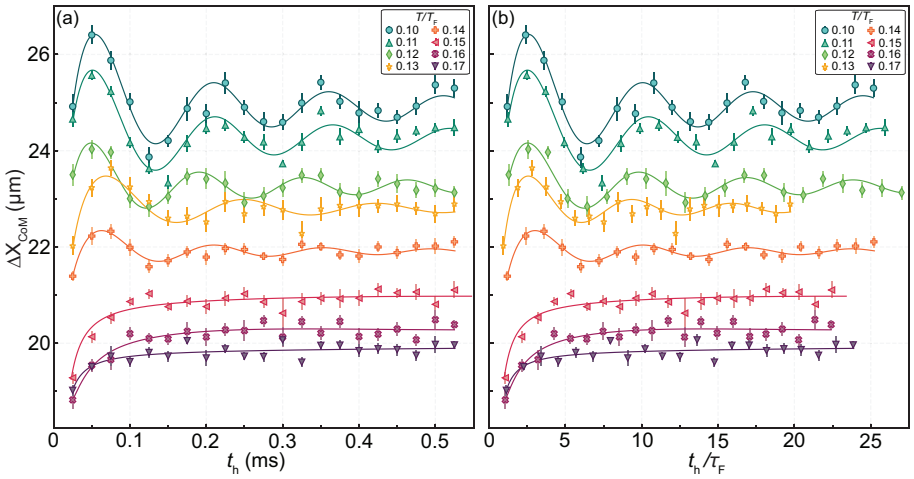

Figure 2: (Color online) A selection of measured centre of mass displacement (ΔX_{CoM}) vs hold time, t_h in absolute units of μs in (a) and relative to the local Fermi time $\tau_F = \hbar/E_F$ in (b) for atom clouds prepared at different temperatures. Also plotted are the fitted sinusoidal functions used to determine the frequency and damping of the amplitude oscillation. Different temperature clouds can have different densities leading to the different absolute oscillation frequencies, (a). When the time axis is taken relative to the Fermi time, (b) the relative frequencies agree more closely, as seen in the main text.

2 Order parameter dynamics within time-dependent BCS theory

We recall here what is theoretically expected for the time evolution of a superfluid Fermi gas after a rapid change of the interatomic interactions at zero temperatures. We consider a two-component ($\uparrow$ and $\downarrow$) Fermi gas interacting through a pairwise single-channel s-wave interaction, which captures broad, entrance-channel dominated Feshbach resonances [12]. Assuming the gas is homogeneous in a cubic volume V (see Sec. 3 for consideration of inhomogeneities in the trapped gas) the momentum representation of the Hamiltonian for this system is

$$\hat{H} = \sum_{\mathbf{k}\sigma} \frac{k^2}{2m} \hat{a}^\dagger_{\mathbf{k}\sigma} \hat{a}_{\mathbf{k}\sigma} + \frac{g_0}{V} \sum_{\mathbf{k},\mathbf{k}',\mathbf{q}} \hat{a}^\dagger_{\mathbf{k}+\mathbf{q},\uparrow} \hat{a}^\dagger_{-\mathbf{k},\downarrow} \hat{a}_{-\mathbf{k}',\downarrow} \hat{a}_{\mathbf{k}'+\mathbf{q},\uparrow}, \tag{2}$$

where the interaction strength g_0 is renormalized to reproduce the correct s-wave scattering length a of the two-body problem. In the remaining sections, we use the convention $\hbar = 1$ throughout.

The equations of motion for the momentum distribution $n_{\mathbf{k}}$ and pairing function $c_{\mathbf{k}}$ (Eqs. (1) and (2) in the main text) are derived from the Hamiltonian in Eq. (2), using the BCS mean-field approximation. At $t = 0$ the system is at equilibrium at scattering length a_i and temperature $T < T_{c,i}$, we can therefore fix the initial conditions for $n_{\mathbf{k}}$ and $c_{\mathbf{k}}$ using the BCS ground-state solutions, as discussed in the main text

$$n_{\mathbf{k}}(t=0) = \frac{1}{2}\left(1 - \frac{\xi_{\mathbf{k},i}}{\epsilon_{\mathbf{k},i}} F_\beta(\epsilon_{\mathbf{k},i})\right), \tag{3}$$

$$c_{\mathbf{k}}(t=0) = -\frac{\Delta_i}{2\epsilon_{\mathbf{k},i}} F_\beta(\epsilon_{\mathbf{k},i}), \tag{4}$$

where $\xi_{\mathbf{k},i} = k^2/2m - \mu_i$, $\epsilon_{\mathbf{k},i} = \sqrt{\xi^2_{\mathbf{k},i} + \Delta_i^2}$, μ_i and Δ_i are calculated at the initial scattering length a_i, and where $F_\beta(\epsilon) = \tanh(\beta\epsilon/2) = 1 - 2(\exp(\beta\epsilon) + 1)^{-1}$ is the thermal distribution with $\beta = 1/k_{\mathrm{B}}T$. The limit of zero temperature corresponds to $F_\beta(\epsilon) \to 1$ for $\epsilon > 0$. Conversely, the regime of temperatures close to the critical temperature T_c is found by taking the limit $\Delta \to 0$ [13].

2.1 Analytical solution in the small-amplitude regime

For shallow quenches, that is, small deviations of $n_{\mathbf{k}}$ and $c_{\mathbf{k}}$ from their equilibrium values, the time-dependent BCS equations (Eqs. (1) and (2) of the main text) can be solved analytically. At zero-temperature, this is a well-studied problem [14–16]. Here we only detail the expression of the normalized amplitude $A_{\rm th}$ of the oscillations (see Eq. (4) of the main text).

In the final equilibrium state (at $a = a_f$ and $T = 0$) and in the modulus-phase basis [17], the linear-response matrix of the order-parameter is given by

$$M(\omega) = \begin{pmatrix} \omega^2 f(\omega) & \omega g(\omega) \\ \omega g(\omega) & (\omega^2 - 4\Delta_f^2) f(\omega) \end{pmatrix}, \tag{5}$$

where Δ_f and μ_f are the gap and chemical potential, respectively, of the final equilibrium state, and we have introduced the functions:

$$f(\omega) = \frac{\Delta_f}{V} \sum_{\mathbf{k}} \frac{1}{2\epsilon_{\mathbf{k}}(\omega^2 - 4\epsilon_{\mathbf{k}}^2)}, \tag{6}$$

$$g(\omega) = \frac{\Delta_f}{V} \sum_{\mathbf{k}} \frac{E_{\mathbf{k}} - \mu_f}{\epsilon_{\mathbf{k}}(\omega^2 - 4\epsilon_{\mathbf{k}}^2)}. \tag{7}$$

The amplitude-amplitude response function introduced in Eq. (3) of the main text follows directly from M through the relation

$$\chi_{|\Delta||\Delta|}(\omega) = (M^{-1}(\omega))_{22} = \frac{f(\omega)}{(\omega^2 - 4\Delta_f^2) f^2(\omega) - g^2(\omega)}. \tag{8}$$

As mentioned in the main text, the imaginary part $\chi''_{|\Delta||\Delta|}$ of this function has a squareroot divergence in $\omega = 2\Delta$ for $\mu_f > 0$ and a square root cancellation for $\mu_f < 0$. We denote by f_l the spectral weight of this squareroot singularity:

$$\chi''_{|\Delta||\Delta|}(\omega) \underset{\omega \to \omega_{\rm th}}{\sim} \begin{cases} f_l \sqrt{\frac{\omega_{\rm th}}{\omega - \omega_{\rm th}}} \text{ when } \mu_f > 0 \text{ and } \omega_{\rm th} = 2\Delta_f \\ f_l \sqrt{\frac{\omega - \omega_{\rm th}}{\omega_{\rm th}}} \text{ when } \mu_f < 0 \text{ and } \omega_{\rm th} = 2\sqrt{\Delta_f^2 + \mu_f^2} \end{cases}. \tag{9}$$

In general, linear response theory expresses time-dependent quantities as Laplace transforms of frequency responses. For the evolution of the amplitude of the order parameter, with initial conditions Eqs. (3) and (4), this gives

$$\frac{\Delta(t) - \Delta_f}{\Delta_i - \Delta_f} = 1 - \frac{1}{\chi_{|\Delta||\Delta|}(0)} \int_{+\infty+i\eta}^{-\infty+i\eta} \frac{e^{-izt}}{2i\pi z} \chi_{|\Delta||\Delta|}(z). \tag{10}$$

This integral is deformed to a contour enclosing the branch cut $[2\Delta, +\infty)$ of $\chi_{|\Delta||\Delta|}$, as well as the pole of the integrand in $z = 0$. Since only the contribution of the pole survives at long times, one sees that $\lim_{t\to+\infty} \Delta(t) - \Delta_f = 0$, in other words

$$\Delta_\infty = \Delta_f \tag{11}$$

in the small-amplitude regime and at $T = 0$. From the contribution of the branch cut we then derive the version of Eq. (4) of the main text that is valid at all times:

$$\frac{\Delta(t) - \Delta_f}{\Delta_i - \Delta_f} = \frac{2}{\pi} \int_{2\Delta_f}^{+\infty} \frac{\cos \omega t}{\omega} \frac{\chi''_{|\Delta||\Delta|}(\omega)}{\chi_{|\Delta||\Delta|}(0)} d\omega. \tag{12}$$

At long times, this frequency integral is evaluated by approximating $\chi''_{|\Delta||\Delta|}$ by its behavior (Eq. (9)) near the pair-breaking threshold. This yields the expression of $A_{\rm th}$ (see Eq. (4) of the main text):

$$A_{\rm th} \underset{T=0}{=} \frac{2 f_l}{\sqrt{\pi} \chi_{|\Delta||\Delta|}(0)} \tag{13}$$

with $\chi_{|\Delta||\Delta|}(0)$ the static modulus response and f_l the spectral weight of the pair-breaking threshold.

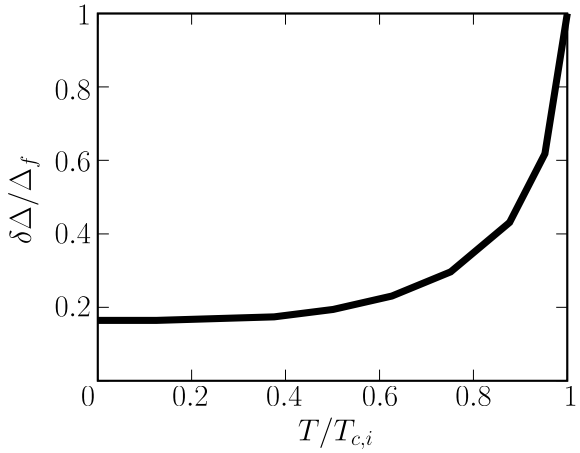

Figure 3: Temperature dependence of the difference in the equilibrium order parameter from the initial and final state $\delta\Delta \equiv |\Delta_f - \Delta_i|$. The initial and final state correspond to $1/(k_F a_i) = -0.18$ and $1/(k_F a_f) = 0$, respectively. The temperature is rescaled by the critical temperature at a_i, that is $T_{c,i} = 0.399 T_F$

.

2.2 Numerical simulations

Outside the small amplitude regime, we evolve the equations of motion (Eqs. (1) and (2) of the main text) using a Runge-Kutta method [18]. The momentum-space integrals in the gap ($\Delta = (g_0/V)\sum_{\mathbf{k}} c_{\mathbf{k}}$) and number ($N = 2\sum_{\mathbf{k}} n_{\mathbf{k}}$) equations are evaluated in spherical coordinates using a fine grid in momentum space[1]. The conservation of the total number of atoms N provides a check on the integrity of the numerics. Similar dynamical problems near resonance have been studied in Refs. [19, 20].

In this section, we consider an infinitely fast quench from $1/(k_F a_i) = -0.18$ to $1/(k_F a_f) = 0$ (see Sec. 3 for a discussion of the nonzero ramping time). As shown in Fig. 3, the relative variation of the equilibrium order parameter is small at $T = 0$ ($\delta\Delta \equiv |\Delta_f - \Delta_i| \approx 0.16\Delta_f$) but increases with temperature, tending to 1 at T_c. Therefore, this limits the applicability of the analytical results presented in Sec. 2.1 to the small temperature regime.

Using numerical simulations, we can instead explore the entire temperature range $0 \leq T \lesssim T_{c,i}$. For example, Fig. 4(a) shows the time evolution of the amplitude of the order parameter Δ at temperature $T = 0.25 T_{c,i}$. As expected from literature (see e.g. Ref. [16] for $T = 0$) and discussed in the main text, the order parameter asymptotes to a value Δ_∞ a bit less than the expected final state equilibrium value Δ_f and oscillates at a frequency $\omega_{\rm H} = 2\Delta_\infty$. Moreover, we expect a power-law damping coefficient $\gamma = 0.5$, which is found if we neglect the very short time dynamics, as shown in Fig. 4(b) for different temperatures. Finally, in Fig. 4(c), we show the temperature dependence of the Higgs oscillation frequency (orange dash-dotted line) and the final order parameter (pink solid), and compare it to the experimental data. The temperature is scaled to the critical temperature of the initial scattering length (for the experimental data we have used $T_{c,i} = 0.15 T_F$). The comparison is not meant to be quantitative, as BCS theory is known to overestimate both the superfluid gap and critical temperature at unitarity [13], but rather to confront the trend in the vicinity of T_c.

[1]Numerically, we evaluate the momentum-space integral of a generic function $f(k)$ using $\int d^3k/(2\pi)^3 f(k) \to \sum_i w_i k_i^2 f(k_i)/2\pi^2$, where k_i and w_i are the abscissas and weights of the Gauss-Legendre quadrature method [18]. Because $n_{\mathbf{k}}$ and $c_{\mathbf{k}}$ become small after a few k_F, we split the integration in two intervals: $[0, 10k_F]$ and $[10k_F, \Lambda]$, where $\Lambda = 350 k_F$ is a momentum cut-off (large enough such that numerical results are insensitive to it). In every interval, we take 1500 points, so that the first interval is much more dense than the second one, where $n_{\mathbf{k}}$ and $c_{\mathbf{k}}$ are ≈ 0.

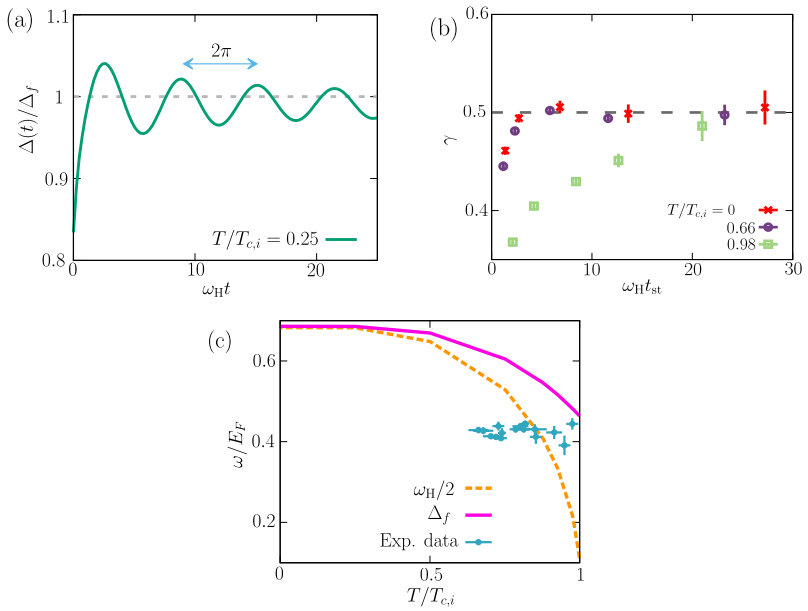

Figure 4: (a) Numerical result for the time evolution of the amplitude of the order parameter $\Delta(t)$ at $T = 0.25T_{c,i}$ after a fast quench from $1/(k_F a_i) = -0.18$ to $1/(k_F a_f) = 0$. The frequency of oscillation is $\omega_H = 2\Delta_\infty \lesssim 2\Delta_f$. (b) Damping coefficient γ for $\Delta(t)$ as a function of the starting point of the fit t_{st} for different temperatures. Here, we have used as a fitting function $\Delta(t) = \Delta_\infty + A\cos(\omega_H t + \phi)/t^\gamma$ in the range $[t_{st}, t_{end}]$, where the final point t_{end} is fixed. (c) Oscillation frequency (dashed dot line) as a function of temperature $T/T_{c,i}$. The dashed (purple) line corresponds to Δ_f in Fermi units. The data points are from the experimental results in Fig. 3(a) of the main text.

3 Application of time-dependent BCS theory to the experimental setup

In this Section, we consider the impact of various experimental effects on the amplitude oscillations and their detection by Bragg spectroscopy. This includes the following: the presence of a nonzero-duration initial ramp of the magnetic field (Sec. 3.1), density inhomogeneities due to the trapping potential (Sec. 3.2), and time averaging over a Bragg pulse of nonzero duration (Sec. 3.3).

3.1 Ramp-rate dependence

To mimic experimental protocols for Feshbach resonances, we include in our numerics an initial linear magnetic field ramp: $B(t) = B_i + Rt$, where $R = dB/dt$ is the ramp rate. The presence of the ramp delays the start of the Higgs oscillation. This delay can be quantified using a timescale $t_q = |B_f - B_i|/R$, which must be compared with the Fermi scale τ_F and the characteristic timescale of the order parameter dynamics $t_\Delta = 1/\Delta$ [21, 22]. When t_q becomes much longer than t_Δ, $|\Delta(t)|$ adiabatically evolves to Δ_f.

We vary the ramp rate R to study its impact on the early-time dynamics of $|\Delta(t)|$. Fig. 5 shows how for slower changes of B (smaller R) the amplitude of the oscillations becomes smaller leading to a decrease in the visibility of the Higgs mode, and the early-time behaviour of $|\Delta|$ has a more parabolic shape that cannot be fitted using a function $\sim \cos(2\Delta t)/\sqrt{t}$ (see Eq. (4) in the main text). In the inset of Fig. 5, we plot the same quantities but we include a delay equal to half ramp time $t_q/2$. Accounting for this delay, acts to align the oscillation phases.

3.2 Inhomogeneous broadening of the signal

As discussed in Sec. 1.1, during the sample preparation, the atoms are loaded into an oblate harmonic potential. In this section, we show how this causes an inhomogeneous broadening of the

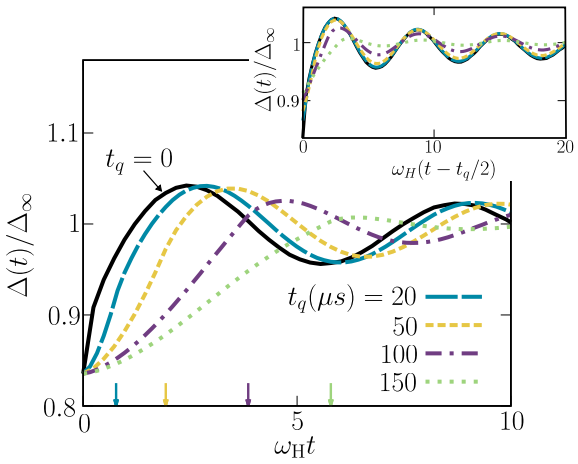

Figure 5: Early-time evolution of the amplitude of the order parameter $\Delta(t)$ after a quench from $1/(k_F a_i) = -0.18$ to $1/(k_F a_f) = 0$ for an infinitely fast ramp (black solid line) and for different ramp time t_q (coloured lines) at zero temperature. We indicate with the bottom coloured arrows, the values of the ramp time t_q corresponding to ramp rate R (see the text). Inset: Same as (a) but the curves are delayed by half the ramp time $t_q/2$.

signal, which can lead to a sharp increase of the damping coefficient γ from 1/2 to 2 depending on the width of the Bragg beam.

We begin by writing the external trapping potential as

$$V_{\rm ho}(\mathbf{r}) = \frac{1}{2} m \left(\omega_r^2 r^2 + \omega_z^2 z^2\right), \tag{14}$$

where ω_r and ω_z are the trapping angular frequencies in the radial and axial directions, respectively [23]. In the local density approximation (LDA), the trapped system can be treated as a collection of locally uniform subsystems[2]. This means that at equilibrium the equation of state for the superfluid can be solved after replacing μ by a local $\mu(\mathbf{r}) = \mu - V_{\rm ho}(\mathbf{r})$ and the number equation becomes

$$N = \int d^3 r n(\mathbf{r}), \tag{15}$$

where $n(\mathbf{r}) = 2\sum_{\mathbf{k}} n_{\mathbf{k}}(\mathbf{r})$ is the local density. Consequently, $\Delta(\mathbf{r})$, $1/(k_F(\mathbf{r})a)$, and $k_{\rm B}T/E_{\rm F}(\mathbf{r})$ also acquire a dependence on $\mathbf{r}$ [25–28]. At unitarity, $1/(k_F(\mathbf{r})a) = +\infty$ becomes uniform, but Δ still depends on $\mathbf{r}$ because $T/T_c(\mathbf{r})$ does.

At zero temperature, for a weakly interacting gas ($|a| \ll k_{\rm F}^{-1}$), $n(\mathbf{r})$ is well-approximated by the Thomas-Fermi distribution:

$$n^{(0)}(\mathbf{r}) = \frac{8N}{\pi^2 R_r^2 R_z}\left[1 - \left(\frac{r}{R_r}\right)^2 - \left(\frac{z}{R_z}\right)^2\right]^{3/2}, \tag{16}$$

where $R_i = \sqrt{2E_F^{\rm ho}/(m\omega_i^2)} = a_{\rm ho}(24N)^{1/6}\omega_{\rm ho}/\omega_i$ ($i = \{r, z\}$) are the Thomas Fermi radii, $\omega_{\rm ho} = (\omega_r^2\omega_z)^{1/3}$ is the geometric mean of the angular frequencies, $a_{\rm ho} = \sqrt{1/(m\omega_{\rm ho})} = (24N)^{1/6}/k_F^{\rm ho}$ is the oscillator length, and $k_F^{\rm ho} = \sqrt{2mE_F^{\rm ho}}$ is the Fermi momentum in a trapped system.

Equation 16 is altered by increasing the scattering length with respect to $k_{\rm F}^{\rm ho}$ as shown in Fig. 6(a), where we compare $n^{(0)}(\mathbf{r})$ with the density profiles for $1/(k_F^{\rm ho}a) = -0.18$ and 0 using the

[2]The local density approximation remains valid while the harmonic oscillator length, which is the typical length at which $n(\mathbf{r})$ varies, is much larger than both the healing length $1/\sqrt{2m\mu}$ and pair correlation length [24] with the latter diverging near T_c as $k_F/m\Delta$, marking an obvious breakdown of the approximation.

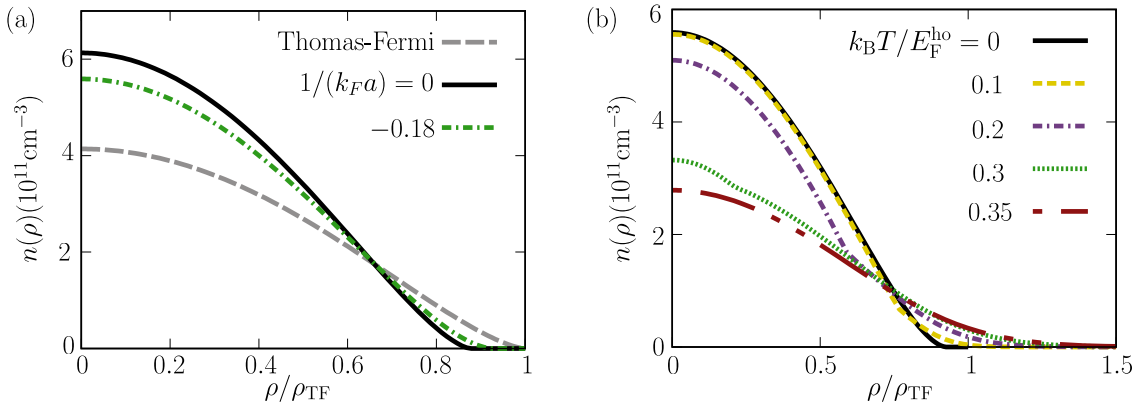

Figure 6: Particle density $n(\rho)$ in a harmonic trap as a function of the weighted radial coordinate ρ in Fermi units. (a) At zero temperature for a non-interacting system (dashed grey), for $1/k_{\mathrm{F}}^{\mathrm{ho}}a = -0.18$ (green dash dotted), and at unitarity (black solid). (b) For fixed $1/(k_{\mathrm{F}}^{\mathrm{ho}}a) = -0.18$ and different temperatures (different colors).

trapping parameters of Sec. 1.1[3]. In Fig. 6, we have utilized the weighted radial coordinate

$$\rho = \frac{\sqrt{(\omega_r r)^2 + (\omega_z z)^2}}{\omega_{\mathrm{ho}}}, \tag{17}$$

with corresponding (rescaled) Thomas-Fermi readius $\rho_{\mathrm{TF}} = \sqrt{2E_{\mathrm{F}}^{\mathrm{ho}}/(m\omega_{\mathrm{ho}}^2)}$. From Fig. 6(a), it is clear that interactions lead to a narrowing of the density distribution. It is noteable that Eq. (17) also shows how the case of a cigar-shape trap can be reduced to the spherical case by homothety. The influence of temperature on the density profile is shown in Fig. 6(b). Deviations from the zero-temperature profile (black solid curve) begin on the edges of the cloud and progress towards the center as temperature is increased.

Within the local density approximation, we use the density distribution $n(\mathbf{r})$ to calculate the global order parameter by averaging over the cloud profile. The spatial weight is the product of the local density, $n(\mathbf{r})$, and local intensity of the probe beam, $I(\mathbf{r})$,

$$\bar{\Delta}(t) = \frac{1}{\bar{n}} \int d^3r n(\mathbf{r}) I(\mathbf{r}) \Delta(\mathbf{r}), \tag{18}$$

such that

$$\frac{1}{\bar{n}} \int d^3r n(\mathbf{r}) I(\mathbf{r}) = 1, \tag{19}$$

where $\bar{n}$ is the mean density. The finite width of the probe beam allows us to consider smaller volumes of the cloud, mimicking the experimental Bragg scheme described in Sec. 1.3. We approximate the probe beam with a Gaussian profile, such that

$$I(\mathbf{r}) = I(0)\, \exp\left(-\frac{|\mathbf{r}|^2}{2\lambda^2}\right), \tag{20}$$

where $I(0)$ is a normalization constant and λ is the effective width of the beam which is fixed to match the experimental mean density (Eq. 1).

Using Eq. (4) of the main text for the time-evolution of Δ, Eq. (18) becomes

$$\bar{\Delta}(t) = \frac{1}{\bar{n}} \int d^3r n(\mathbf{r}) I(\mathbf{r}) \left(\Delta_\infty(\mathbf{r}) + \frac{\cos(2\Delta(\mathbf{r})t + \phi)}{\sqrt{\nu(\Delta(\mathbf{r}))t}}\right). \tag{21}$$

[3]When $a \to \infty$, the dimensionless parameter $1/(k_F(\mathbf{r})a)$ loses spatial dependence, and the equation of state for the Fermi gas is expected to be universal in terms of density scales and is written in terms of the Bertsch parameter ξ_{B} [13, 29]. Therefore, using $\mu(\mathbf{r})/E_F(\mathbf{r}) = \xi_{\mathrm{B}}$ and Eq. 16, the density profile can be approximated by $n(\mathbf{r}) = \xi_{\mathrm{B}}^{-3/2} n^{(0)}(\mathbf{r})$, which well describes experimental data in the unitary regime when a beyond-mean field ξ_{B} is used [30].

with the rewriting of the oscillation amplitude $\nu = 2\Delta/(A_{\rm th}(\Delta_i - \Delta_\infty))^2$. The density average of functions oscillating at frequencies $2\Delta(\mathbf{r})$ leads to a blurring of the Higgs signal and consequently to a reduced contrast of the oscillations.

3.2.1 Qualitative discussion in the limit of a tightly focused beam

When the beam is well focused around the center of the trap, one can approximate the density using

$$n(\rho) = n_0 - \alpha\rho^2, \tag{22}$$

with $\alpha = -(1/2)d^2n/d\rho^2$ (see Eq. (16)). The small variation of the density around trap center causes a spatial variation of the order parameter $\Delta(\rho) = \Delta_0 - \Delta'\alpha\rho^2$, and of the magnitude of the Higgs oscillations $\nu(\rho) = \nu_0 - \nu'\alpha\rho^2$ (where $\Delta' = d\Delta/dn$ and $\nu' = d\nu/dn$). To simplify the discussion, we consider here only a probe which respects the cylindrical symmetry of the trapping potential $I(\mathbf{r}) = I(\rho)$, as defined in Eq. (20). This leads to

$$\bar{\Delta}(t) = \bar{\Delta}_\infty + \frac{4\pi n_0}{\bar{n}\sqrt{\nu_0 t}} \int_0^{+\infty} \rho^2 d\rho I(\rho)(1 - c\rho^2)\cos(2\Delta_0 t - \Delta'\alpha\rho^2 t + \phi), \tag{23}$$

where the term proportional to $c = \alpha(1/n_0 - \nu'/2\nu_0)$ is included for completeness but becomes negligible when the beam waist tends to 0. In this approximation, the averages of slowly-varying quantities simply coincide with their value at the center of the trap ($\bar{n} = n_0$, $\bar{\nu} = \nu_0$ etc.), and only the average of the oscillatory part remains.

Performing the radial integral in Eq. (23) for the Gaussian profile Eq. (20) gives

$$\bar{\Delta}(t) = \bar{\Delta}_\infty + \frac{1}{\sqrt{\nu_0 t}} \mathrm{Re}\left[e^{2i\Delta_0 t + i\phi} f(t)\right], \tag{24}$$

where the complex-valued blurring function

$$f(t) = \left(\frac{1 - it/t_{\rm d}}{1 + t^2/t_{\rm d}^2}\right)^{3/2} \tag{25}$$

depends on the characteristic timescale

$$t_{\rm d} = \frac{1}{4\lambda^2\alpha\Delta'} \approx \frac{1}{\Delta(\lambda) - \Delta_0} \tag{26}$$

Assuming that this timescale is large ($\Delta_0 t_{\rm d} \gg 1$), the Higgs oscillations will still display the expected $1/\sqrt{t}$ attenuation law at short times ($t \ll t_{\rm d}$). However, beginning at $t \approx t_{\rm d}$ the decay is quickened and the phase shifts from the original $\phi = \pi/4$ phase. At later times ($t \gg t_{\rm d}$), one finds instead a $1/t^2$ attenuation law:

$$\bar{\Delta}(t) \underset{t\to+\infty}{\simeq} \bar{\Delta}_\infty - \frac{t_{\rm d}^{3/2}}{\sqrt{\nu_0} t^2} \sin 2\Delta_0 t. \tag{27}$$

This shows that inhomogeneous broadening can seriously impair the observation of the power-law damping exponent $\gamma = 1/2$ or $3/2$.

3.2.2 Numerical solutions in the general case

More generally, we solve numerically[4] Eq. (18) for different values of λ and, consequently, for different $\bar{n}$. Fig. 7 shows the evolution of the superfluid order parameter at zero temperature after

[4]To perform the integration in Eq. 18, we sample $n(\mathbf{r})$ using a "accept-reject method" [31], which generates a set of random numbers distributed according to the initial distribution: $n(\mathbf{r}) \to \{n_i$, with $i = 1, \cdots, N_{\rm p}\}$. The average on Eq. 18 can be then performed using

$$\bar{\Delta}(t) = \frac{1}{\sum_i^{N_{\rm p}} I(n_i)} \sum_{i=1}^{N_{\rm p}} I(n_i)\Delta(n_i, t), \tag{28}$$

where $N_{\rm p}$ is the total of number of extracted values n_i.

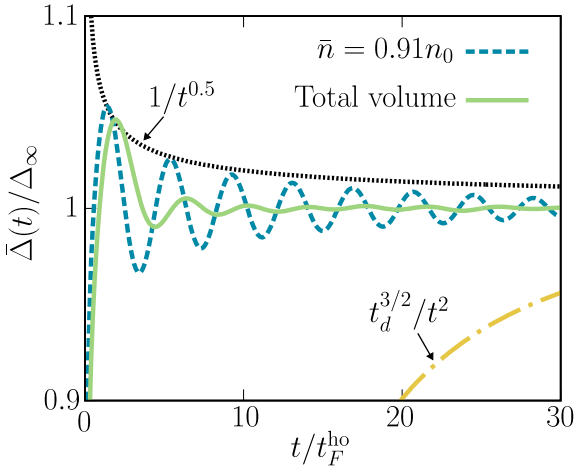

Figure 7: Time evolution of the order parameter after averaging over the total density profile of the trap (green solid line) and over a reduced volume with corresponding $\bar{n} = 0.91n_0$ (blue dashed line) at zero temperature. Black dotted and yellow dashed dotted lines indicate the power law curves $1/\sqrt{t}$, which is found at short times, and $1/t^2$ from Eq. 27, which characterizes longer times than the maximum time in the figure ($t \gg t_{\rm d}$).

a quench from $1/k_F^{\rm ho}a = -0.18$ to unitarity after averaging over a probe beam of width $\lambda = 0.06\rho_{\rm TF}$ such that $\bar{n} = 0.91n_0$, compared to the case where the probe beam covers the entire volume. We observe that this latter case yields strongly-damped oscillations, which would be difficult to observe. Instead, the experimentally-relevant average over a smaller volume leads to distinct oscillations. Moreover, because $\lambda = 0.06\rho_{\rm TF}$ is small compared to the effective Thomas-Fermi radius $\rho_{\rm TF}$, the characteristic time t_d is much larger than the oscillation period $2\pi/\omega_{\rm H}$, and therefore, for times $t < t_{\rm d}$, we do not expect the attenuation law $1/t^2$ (as described by Eq. (27)) to play a role within the experimentally relevant time window.

We address also the impact of inhomogeneous broadening on the damping law in the time region $0 < t < t_{\rm d}$. Fig. 8 shows trends in the local oscillation maxima $\bar{\Delta}(t_n)$ at discrete times t_n measured in units of the oscillation frequency $\omega_{\rm H}$ and at temperature $T = 0.66T_{\rm c,i}$. We fit the first few oscillations to a power-law damping, thereby mimicking the analysis performed on the experimental data. For smaller values of λ compared to $\rho_{\rm TF}$, the power law decay $1/\sqrt{t}$ is still a good fit for the short-time behavior of $\bar{\Delta}$, as shown by the case with $\bar{n} = 0.98n_0$ in Fig. 8. For larger values of λ, we find an intermediate behavior, characterized by a power-law decay $1/t^\beta$ with $0.5 < \beta < 2.0$.

3.3 Averaging over the Bragg time

Experimental measurements are taken using two-photon Bragg scattering as illustrated in Fig. 1 of the main text. To avoid over-broadening the sharp features of the response function, the duration $t_{\rm B} = 50\mu s$ of the Bragg pulse should be as long as possible. However, in an out-of-equilibrium system, using pulses that are too long allows the system to evolve significantly during the probe time violating the timescale separation assumptions underlying Eq. (5) of the main text and possibly blurring the oscillatory signal. Explicitly, the observable Δ reported at the time t is actually the result of a time-average:

$$\langle \Delta(t) \rangle_{\rm Bragg} = \frac{1}{t_{\rm B}} \int_{t-t_{\rm B}/2}^{t+t_{\rm B}/2} \Delta(t')dt'. \tag{29}$$

Fig. 9 shows the comparison between the time-evolution of (spatially-averaged) Δ for $t_B = 0$ and $t_B = 50\mu s$. Although the time-averaging reduces the contrast of the oscillations by reducing their the magnitude, it is less critical than the spatial averaging as it does not affect the attenuation law.

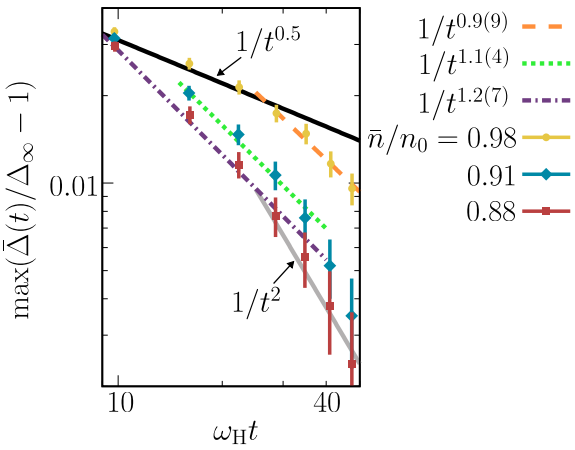

Figure 8: Data points: Maximum values of $(\bar{\Delta}(t)/\Delta_\infty - 1)$ for different $\bar{n}$ or equivalently λ at $T = 0.66 T_{\rm c,i}$. The solid black line represents the homogeneous power-law behavior $1/\sqrt{t}$ (see Eq. (4) in the main text). Dashed lines: Fitting functions $1/t^\beta$ for times $t < t_d$. Gray solid line: power law $1/t^2$ recovered only in the case with lower $\bar{n}$.

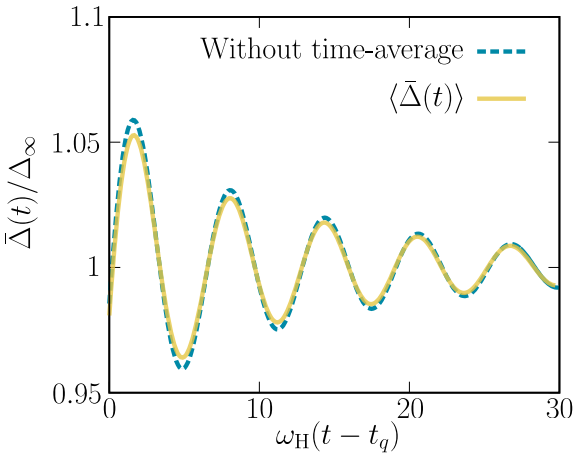

Figure 9: Comparison between the time and space averaged order parameter ($\langle\bar{\Delta}(t)\rangle$, yellow solid line) and the same quantity only averaged over space ($\bar{\Delta}(t)$, blue dashed line). The time average is performed over the Bragg time $t_{\rm B}$ (see Eq. (29)) and the density average corresponds to the case $\bar{n} = 0.91 n_0$ (see Eq. (18)). The temperature is $T = 0.66 T_{\rm c,i}$.

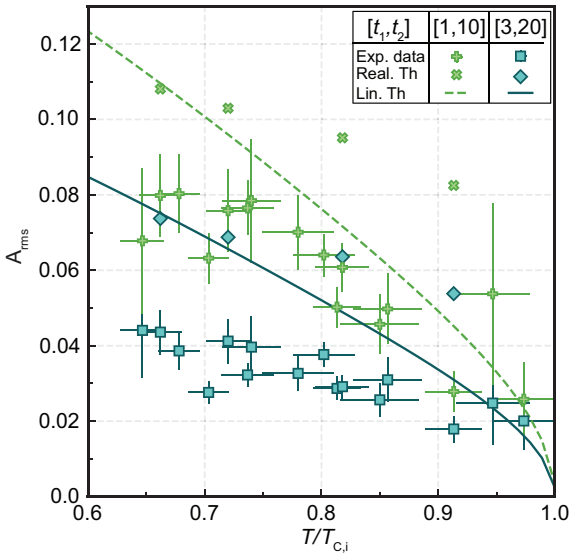

Figure 10: Comparison between the theoretical (diamonds and x's) and experimental (squares and plus) averaged magnitudes of the oscillations, $A_{\rm rms}$, in two different time ranges in units of $\tau_{\rm H}$. Shown as dashed-dotted lines is the magnitude of the oscillations obtain by integrating Eq. (12), that is, in the linear regime and without any of the experimental effects discussed in Sec. 3.

4 Comparing theoretical predictions and experimental measurements

The comparisons with experiment shown in Figs. 2(b) and 3(b) of the main text use theoretical predictions for $\langle\bar{\Delta}(t)\rangle$ that combine both the spatial and temporal averages discussed in Secs. 3.2 and 3.3 and the dephasing introduced by the finite ramp time t_q discussed in Sec. 3.1. From Eq. (5) of the main text, we write the experimental signal as $S(t) \approx \alpha + \beta\Delta(t)$, where α and β depend on the sensitivity with an explicit expression of those quantities given below. This dependency is removed by taking the ratio

$$\frac{S(t) - S_\infty}{S_f - S_i} \sim \frac{\langle\bar{\Delta}(t)\rangle - \Delta_\infty}{\Delta_f - \Delta_i}. \tag{30}$$

To avoid the well-known overestimation of BCS theory of the critical temperature T_c and superfluid gap Δ, we compare theoretical predictions and experiment signal as a function of $\omega_{\rm H}t$ and $T/T_{c,i}$ using experimental values of $\omega_{\rm H}/\epsilon_F$, fitted from the bare experimental signal, and $T_{c,i}/T_F$, estimated as the temperature at which Higgs oscillations are no longer observed.

4.1 Magnitude averaged over different time windows

To quantify the agreement between experiment and theory, we compute at each temperature the root-mean-square of the signal (30):

$$A_{\rm rms} = \sqrt{\frac{1}{t_2 - t_1}\int_{t_1}^{t_2} {\rm d}t \left(\frac{S(t) - S_\infty}{S_f - S_i}\right)^2}, \tag{31}$$

As discussed in the main text, the choice of the averaging time window $[t_1, t_2]$ significantly affects the gap between measurements and theoretical predictions, the best agreement being found at early times. In Fig. 10, we show that the agreement is better from $[t_1, t_2] = [\tau_{\rm H}, 10\tau_{\rm H}]$ than in the window $[3\tau_{\rm H}, 20\tau_{\rm H}]$ used in the main text.

4.2 Comparisons including the sensitivity of the Bragg pulse

In this subsection, we predict the experimental Bragg signal from our calculation of the density-density response within the Random Phase Approximation (RPA), that is, without scaling out

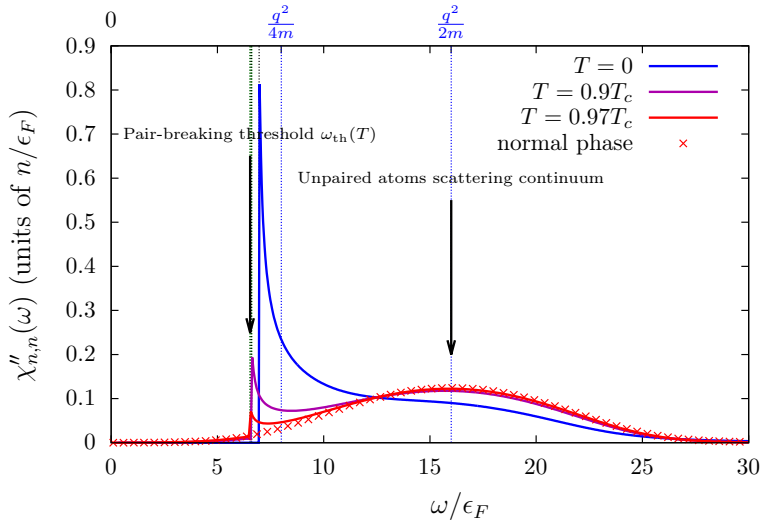

Figure 11: The imaginary part of the density-density response function χ_{nn} in density units as a function of the excitation frequency ω at fixed excitation wave number $q = 4k_F$ and temperature varying from $T = 0$ (blue curves), $T = 0.9T_c$ (purple curves) to $T = 0.97T_c$ (red curves). The threshold of the pair-breaking continuum (black dotted vertical lines, given by Eq. (33)) is sensitive to the value of Δ and thus depends slightly on temperature, tending to $2(q^2/8m - \mu)$ in the limit $T \to T_c$ where $\Delta \to 0$. For comparison, we show the kinetic energy of atoms (mass m) and pairs (mass $2m$) in vacuum (blue vertical dotted lines, independent of T). At the pair-breaking threshold, χ_{nn} has a sharp peak indicating resonance with the condensed pairs. As temperature increases, the number of pairs decreases in favor of unpaired atoms. This results in a decreased spectral weight of the peak at $\omega_{\rm th}$ and correspondingly in a growth of a broad single-atom scattering continuum centered around $\omega = q^2/2m$. This broad peak is due to the imaginary part of the normal density-density propagator Π_{nn} (see Eq. (46) in [34]) which is shown by the red crosses at the highest temperature $T = 0.97T_c$. These curves are drawn at unitarity ($1/|a| = 0$) which corresponds at $T = 0$ and with the mean-field equation-of-state to $\mu/\Delta \simeq 0.86$ and $\epsilon_F/\Delta \simeq 1.46$. At $T = T_c$, this corresponds to $\mu(T_c)/T_c = 1.50448$, $\epsilon_F(T_c)/T_c \simeq 0.89$.

the sensitivity. As discussed in the main text (see Eq. (5)), the Bragg signal is sensitive to the variations of $\Delta(t)$ through the dimensionless sensitivity

$$\sigma = \frac{\Delta}{\chi_{nn}} \left(\frac{\partial \chi_{nn}}{\partial \Delta} \right)_{n,T}, \tag{32}$$

This thermodynamic quantity is computed by comparing equilibrium states having the same equilibrium density and temperature but slightly different values of the order parameter Δ (or equivalently, slightly different values of the scattering length a). The calculation of χ_{nn} within RPA is a standard problem [32, 33]. In practice we have used the explicit expressions of Ref. [34] (see in particular Eqs. (36) and (46) therein) to evaluate numerically χ_{nn} as a function of the excitation frequency ω and wavevector q.

To illustrate how the density-density response is sensitive to Δ, Fig. 11 shows $\chi_{nn}(\omega)$ in the regime of large excitation wavevector ($q = 4k_F$) used in the experiment. The feature which characterizes the superfluid phase is a sharp edge at the pair-breaking threshold:

$$\omega_{\rm th} = 2\sqrt{\Delta^2 + \left(\frac{q^2}{8m} - \mu \right)^2} \quad (\text{for } q^2/8m > \mu). \tag{33}$$

As this threshold location changes with Δ, the density response χ_{nn} for fixed ω/ϵ_F varies sharply. However, as temperature increases towards T_c, the spectral weight of the edge drops in favor of the broad atomic scattering continuum, characteristic of the ideal (normal) Fermi gas. This fading of the pair-breaking edge consequently reduces the sensitivity σ.

In theory, the vertical tangent of $\omega \mapsto \chi_{nn}(\omega, \Delta)$ in $\omega_{\rm th}^+$, causes a divergence[5] of the sensitivity at the edge (see the blue curve in Fig. 12), which should favor the detection of Higgs oscillations. In practice, the finite duration of the Bragg pulse limits the spectral resolution on χ_{nn}, thereby limiting the maximal accessible value of the sensitivity to roughly $\sigma \lesssim 2$ (red curve in Fig. 12). This is obtained by broadening χ_{nn} according to the convolution formula

$$\chi_{nn}^{\rm br}(\omega_0) = \int_{-\infty}^{+\infty} {\rm d}\omega \chi_{nn}(\omega) f_{\delta\omega}(\omega_0 - \omega) \tag{34}$$

where $f_{\delta\omega}(\omega)$ is a broadening function parametrized by its energy-width $\delta\omega$. In the comparison performed in Fig. 13 we have taken $\delta\omega/\epsilon_F = \tau_{\rm F}/t_{\rm B} \simeq 0.55$, using the Fermi time $\tau_{\rm F} \simeq 27.4402\mu s$ associated to the density in the trap center at unitarity, and a Gaussian broadening profile:

$$f_{\delta\omega}(\omega) = \frac{1}{\sqrt{2\pi}\delta\omega} {\rm e}^{-\omega^2/2(\delta\omega)^2}. \tag{35}$$

However the choice of a Gaussian broadening profile is not crucial for this discussion. Compared to our previous experimental schemes [35], the spectral width is relatively larger here, due to the necessity of maintaining a Bragg duration much smaller than $2\pi/\omega_{\rm H}$. As visible in Fig. 12, the selected excitation frequency $\omega = \hbar^2 q^2/4m$ is fairly optimal for the broadened sensitivity whereas $\omega = \omega_{\rm th}$ is preferable in the absence of broadening.

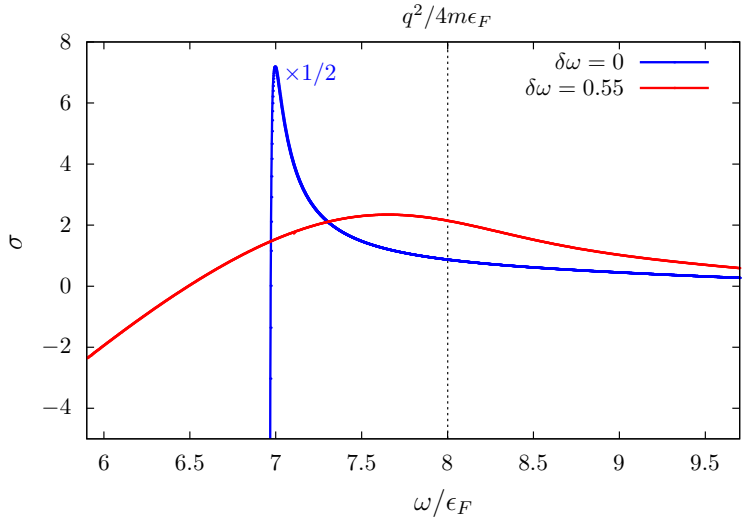

Figure 12: The bare (blue curve) and broadened (red curve) sensitivities as a function of the excitation frequency for $q = 4k_F$, $T = 0$, and $1/k_F a = 0$.

Using the sensitivity (32), we directly predict the scaled Bragg response $S(t)/S_\infty$ from

$$\frac{\langle \bar{\chi}''_{nn}(t)\rangle}{\bar{\chi}''_{nn}(+\infty)} = 1 + \sigma_f \frac{\Delta_\infty}{\Delta_f}\left(\frac{\langle \bar{\Delta}(t)\rangle}{\Delta_\infty} - 1\right), \tag{36}$$

where we have assumed that the width of the Bragg laser λ is small enough such that the dependence of the sensitivity $\sigma_f \equiv \sigma(\Delta_f)$ on $\mathbf{r}$ can be neglected. Note that the linearization of χ_{nn} performed in Eq. (36) is valid only in the small amplitude approximation, hence at low T/T_c.

In Fig. 13, we compare the theoretical curve Eq. (36) to the experimental measurements of $S(t)/S_\infty$. We consider the lowest temperature case, $T = 0.10T_F$, for which $\delta\Delta$ is small enough

[5] To understand this divergence and also to obtain rigorous numerical results for the blue curve in Fig. 12, we write $\chi_{nn}(\omega, \Delta) = \Theta(\omega - \omega_{\rm th}(\Delta)) f(\omega - \omega_{\rm th}(\Delta), \Delta)$ where the function $\delta\omega \mapsto f(\delta\omega, \Delta)$ is defined on $[0, +\infty[$. Taking the derivative with respect to Δ (and using $f(0, \Delta) = 0$), we have $\partial\chi_{nn}/\partial\Delta = \partial f/\partial\Delta - ({\rm d}\omega_{\rm th}/{\rm d}\Delta) \times (\partial f/\partial\delta\omega)$. The vertical tangent of χ_{nn} in $\omega_{\rm th}^+$ implies a divergence of $\partial f/\partial\delta\omega$ in $\delta\omega = 0^+$, and therefore a divergence of the sensitivity.

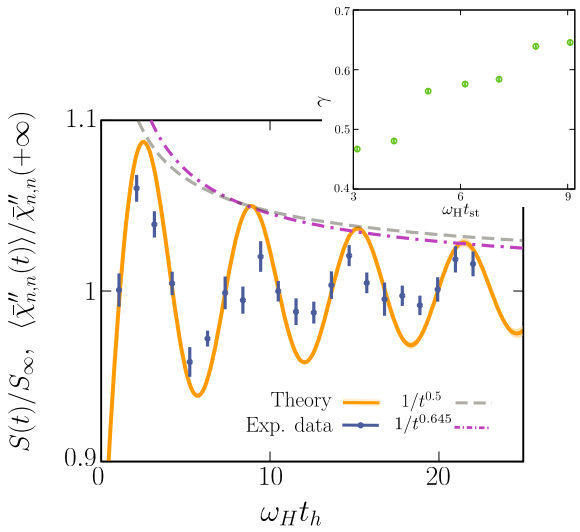

Figure 13: Comparison between the experimental Bragg signal $S(t)/S_\infty$ and its theoretical prediction Eq. (36). The theoretical curve has been obtained at fixed $T = 0.66T_{c,i}$ by including a linear ramp in $50\mu s$ with $t_h = t - t_q/2$ corresponding to the theoretical delay found in Sec. 3.1, the inhomogeneous broadening, the Bragg time averaging, and the Fourier broadening. The experimental points correspond to $T = 0.10T_F$ and the mean density is $\bar{n} = (0.955 \pm 0.018)n_0$ (see main text). We show the deviation from the $1/t^{0.5}$ power-law damping (grey dashed line). The power-law $1/t^{0.645\pm0.005}$ (dashed-dotted purple curve) has been obtained by fitting the theoretical curve in the time range $9 \leq \omega_H t_h \leq 23$ (from the second peak to the last experimental point). Inset: Damping coefficient as a function of the starting time $t_{\rm st}$ of the fitting window used for the theoretical curve.

with respect to Δ_f to justify the use of the small-amplitude regime (we have $|\Delta_\infty - \Delta_f| \simeq 0.11\Delta_f$). At the latest times considered in the experiments, we find a small deviation of our theoretical prediction from the homogeneous $1/t^{1/2}$ power-law damping, with γ increasing to 0.645 ± 0.005. This deviation could be seen if we exclude the first peak of the oscillation from the theoretical fitting window, consistently with our analysis in Sec. 3.2 (compare with Fig. 8 and the inset of Fig. 13). Instead, using the experimental fitting window, which also includes the first peak, this deviation is nearly compensated, as discussed in the main text.

References

[1] N. L. Smith, W. H. Heathcote, G. Hechenblaikner, E. Nugent, and C. J. Foot, Journal of Physics B: Atomic, Molecular and Optical Physics **38**, 223 (2005).

[2] S. P. Rath, T. Yefsah, K. J. Günter, M. Cheneau, R. Desbuquois, M. Holzmann, W. Krauth, and J. Dalibard, Phys. Rev. A **82**, 013609 (2010).

[3] P. Dyke, K. Fenech, T. Peppler, M. G. Lingham, S. Hoinka, W. Zhang, S.-G. Peng, B. Mulkerin, H. Hu, X.-J. Liu, and C. J. Vale, Phys. Rev. A **93**, 011603(R) (2016).

[4] G. Zürn, T. Lompe, A. N. Wenz, S. Jochim, P. S. Julienne, and J. M. Hutson, Phys. Rev. Lett. **110**, 135301 (2013).

[5] P. Dyke, A. Hogan, I. Herrera, C. C. N. Kuhn, S. Hoinka, and C. J. Vale, Phys. Rev. Lett. **127**, 100405 (2021).

[6] M. J. H. Ku, A. T. Sommer, L. W. Cheuk, and M. W. Zwierlein, Science **335**, 563 (2012).

[7] S. Hoinka, P. Dyke, M. G. Lingham, J. J. Kinnunen, G. M. Bruun, and C. J. Vale, Nature Physics **13**, 943 (2017).

[8] C. Carcy, S. Hoinka, M. G. Lingham, P. Dyke, C. C. N. Kuhn, H. Hu, and C. J. Vale, Phys. Rev. Lett. **122**, 203401 (2019).

[9] M. G. Lingham, K. Fenech, S. Hoinka, and C. J. Vale, Phys. Rev. Lett. **112**, 100404 (2014).

[10] G. Veeravalli, E. Kuhnle, P. Dyke, and C. J. Vale, Phys. Rev. Lett. **101**, 250403 (2008).

[11] C. A. Regal, M. Greiner, and D. S. Jin, Phys. Rev. Lett. **92**, 040403 (2004).

[12] C. Chin, R. Grimm, P. Julienne, and E. Tiesinga, Rev. Mod. Phys. **82**, 1225 (2010).

[13] G. C. Strinati, P. Pieri, G. Röpke, P. Schuck, and M. Urban, Physics Reports **738**, 1 (2018).

[14] A. Volkov and S. M. Kogan, Zh. Eksp. Teor. Fiz **65**, 2038 (1973).

[15] V. Gurarie, Phys. Rev. Lett. **103**, 075301 (2009).

[16] E. A. Yuzbashyan, M. Dzero, V. Gurarie, and M. S. Foster, Phys. Rev. A **91**, 033628 (2015).

[17] H. Kurkjian, S. N. Klimin, J. Tempere, and Y. Castin, Phys. Rev. Lett. **122**, 093403 (2019).

[18] W. H. Press, B. P. Flannery, S. A. Teukolsky, W. T. Vetterling, *et al.*, *Numerical Recipes*, Vol. 3 (Cambridge University Press, Cambridge, 1989).

[19] M. Holland, S. J. J. M. F. Kokkelmans, M. L. Chiofalo, and R. Walser, Phys. Rev. Lett. **87**, 120406 (2001).

[20] S. J. J. M. F. Kokkelmans, J. N. Milstein, M. L. Chiofalo, R. Walser, and M. J. Holland, Phys. Rev. A **65**, 053617 (2002).

[21] R. A. Barankov, L. S. Levitov, and B. Z. Spivak, Phys. Rev. Lett. **93**, 160401 (2004).

[22] R. G. Scott, F. Dalfovo, L. P. Pitaevskii, and S. Stringari, Phys. Rev. A **86**, 053604 (2012).

[23] L. Pitaevskii and S. Stringari, *Bose-Einstein Condensation and Superfluidity*, Vol. 164 (Oxford University Press, 2016).

[24] M. Marini, F. Pistolesi, and G. Strinati, The European Physical Journal B **1**, 151–159 (1998).

[25] A. Perali, P. Pieri, and G. C. Strinati, Phys. Rev. A **68**, 031601 (2003).

[26] L. Salasnich, N. Manini, and A. Parola, Phys. Rev. A **72**, 023621 (2005).

[27] M. L. Chiofalo, S. J. J. M. F. Kokkelmans, J. N. Milstein, and M. J. Holland, Phys. Rev. Lett. **88**, 090402 (2002).

[28] R. Haussmann and W. Zwerger, Phys. Rev. A **78**, 063602 (2008).

[29] T.-L. Ho, Phys. Rev. Lett. **92**, 090402 (2004).

[30] A. Perali, P. Pieri, and G. C. Strinati, Phys. Rev. Lett. **93**, 100404 (2004).

[31] W. Krauth, *Statistical Mechanics Algorithms and Computations* (Oxford University Press, Oxford, 2006).

[32] G. M. Bruun and B. R. Mottelson, Phys. Rev. Lett. **87**, 270403 (2001).

[33] A. Minguzzi, G. Ferrari, and Y. Castin, The European Physical Journal D **17**, 49–55 (2001).

[34] H. Kurkjian, J. Tempere, and S. N. Klimin, Scientific Reports **10(1)**, 11591 (2020).

[35] S. Hoinka, P. Dyke, M. G. Lingham, J. J. Kinnunen, G. M. Bruun, and C. J. Vale, Nature Physics **13**, 943 (2017).